Optical trapping of spheroidal particles in Gaussian beams

Stephen H. Simpson and Simon Hanna

H. H. Wills Physics Laboratory, University of Bristol, Tyndall Avenue, Bristol, BS8 1TL, UK

Received April 10, 2006; revised July 5, 2006; accepted August 1, 2006;
posted August 25, 2006 (Doc. ID 69820); published January 10, 2007

The T matrix method is used to compute equilibrium positions and orientations for spheroidal particles trapped in Gaussian light beams. It is observed that there is a qualitative difference between the behavior of prolate and oblate ellipsoids in linearly polarized Gaussian beams; the former generally orient with the symmetry axis parallel to the beam except at very small particle sizes, while the latter orient with the symmetry axis perpendicular to the beam. In the presence of a circularly polarized beam, it is demonstrated that oblate ellipsoids will experience a torque about the beam axis. However, for a limited range of particle sizes, where the particle dimensions are comparable with the beam waist, the particles are predicted to rotate in a sense *counter* to the sense of rotation of the circular polarization. This unusual prediction is discussed in some detail.

OCIS codes: 140.7010, 290.5850.

1. INTRODUCTION

Since their introduction in the 1980s,[1] optical tweezers have found extensive applications from fundamental studies of the properties of light to the manipulation of biological structures.[2] With the introduction of high-quality spatial light modulators, holographic optical tweezers have become a reality,[3] and systems are now being developed capable of generating and controlling large arrays of optical traps. In a previous paper,[4] we described a method, based on T matrix theory, for calculating the forces on and between spherical particles in multiple optical traps. In this paper, we explore the forces and torques operating during the optical trapping of spheroidal particles.

A spheroid is defined as an ellipsoid with uniaxial symmetry or, alternatively, as a sphere that has been uniformly deformed parallel to one axis. One example of this that has appeared in the optical trapping literature is the chloroplast, which may be modeled as an oblate spheroid.[5] The symmetry axis of the spheroid is referred to variously as the unique, primary, or principal axis. In fact, a general ellipsoid has two other principal axes, which in the case of the spheroid, will be equal in length. We will refer to these as the secondary axes. The aspect ratio of the spheroid δ is given by

$$\delta = a/b, \tag{1}$$

where a and b are the lengths of the primary and secondary axes, respectively. We will consider the trapping of both prolate spheroids, for which $\delta > 1$, and oblate spheroids, where $\delta < 1$.

Optical trapping of spherical particles is well understood and has been extensively documented both in terms of experimental observation and in terms of theoretical analysis.[6–8] Qualitative discussion of the phenomenon frequently involves expressions such as gradient force, scattering force, and radiation pressure, each of which serves to describe a different aspect of the changes in electromagnetic momentum that take place as a result of the scattering of light from a particle. (N.B. we use the term "radiation pressure" to denote the force associated with the net flow of electromagnetic energy down the beam and not the total pressure, as used by some authors). An analogous vocabulary does not exist for the description of torque-related phenomena. This is unfortunate, since it is the induced torque that is responsible for the equilibrium orientation of a spheroidal particle in a laser beam.

A helpful principle to bear in mind is one that forms the basis of the theory of optical waveguides; it is often energetically favorable for the overlap between the refractive index distribution and the light intensity to be maximized, hence the propensity of light to be confined to the guide. This idea gives rise to the concept of gradient force and in the case of geometrically anisotropic particles suggests that an elongated particle will tend to align itself in an elongated intensity distribution (such as that furnished by a Gaussian beam), and that optical torques will be exerted in order to achieve this arrangement.

A second principle that has a part to play in the trapping of spheroidal particles is related to the fact that, in the quasi-static limit, i.e., for particles much smaller than a wavelength, the scattering properties of an ellipsoid can be expressed in terms of a polarizability tensor.[9] The potential energy of an anisotropic point polarizability in an electromagnetic field is minimized by aligning the eigenvector corresponding to the highest eigenvalue of the polarizability tensor parallel to the polarization vector of the electric field.[10] While the quasi-static limit does not generally pertain in the present case, the behavior might be expected to be mimicked to some extent.

A number of experimental studies of anisotropic systems have been performed. For example, Bishop *et al.*[11] and Bonin *et al.*[12] have observed the reorientation of the

long axis of a microcylinder toward the polarization direction of the incident beam for particles lying close to a horizontal interface. Similar orientational properties have been observed for flat, cross-shaped particles by Galajda and Ormos.[13] Analogous effects have also been observed for particles whose anisotropy stems from their refractive index as opposed to their shape. For example, experiments performed by La Porta and Wang[14] show that near-spherical quartz particles tend to align their optic axes with the polarization vector of the electric field by virtue of their small, positive birefringence.

There are a number of different approaches that could be adopted in gaining theoretical insight into the phenomena outlined above. This is reflected in the variety of computational methods that have been employed in the literature. For length scales greatly in excess of one wavelength, optical interactions can be approximated by a ray-based model, as demonstrated by Kim and Kim.[15] Another approach involves the calculation of radiation pressures by considering photon flux equations.[16,17] Both of these methods have their own advantages and disadvantages and rely on the appropriate conditions pertaining. For example, the ray-tracing approach assumes that interfaces are approximately flat on the wavelength scale, which limits the size of scattering bodies that can be considered. Inaccurate answers may also be obtained for small particles using the photon flux model, since multiple reflections are not generally included.

In the present paper, the T matrix method[18,19] is employed; the particles considered will be both prolate and oblate spheroids of an optically isotropic material, i.e., silica glass. The T matrix method involves an expansion of the incident and scattered fields in the trap as a series of orthogonal vector spherical harmonics. The expansion coefficients of the scattered field are given by a linear transformation of the incident field coefficients, the transformation being determined by the boundary condition on the surface of the scatterer. In theory, the method provides exact solutions to Maxwell's equations, the only approximation being the truncation of the series expansions for the various fields. The method has been employed previously by Bishop *et al.*[11] to calculate the optical torques on cylindrical particles. In a previous paper, we used T matrices to calculate the forces arising between pairs of spherical particles in optical traps.[4] Here, we use a similar method to calculate equilibrium trapping positions and orientations for a range of spheroids with different aspect ratios and examine the stability of their equilibrium positions with respect to translational and orientational perturbations. We also use hydrodynamic theory, through the use of friction tensors, to convert the calculated forces and torques to linear and angular velocities. However, the effect of Brownian motion will be reserved for a future publication.

2. DETAILS OF THE CALCULATION METHOD

Extensive accounts of T matrix theory may be found elsewhere.[18,19] Some of the details of the implementation used in producing the following results were given previously.[4] A brief summary is included here.

As mentioned above, the scattering process is incorporated into T matrix theory by way of a linear transformation; the matrix representing this transformation has elements determined by the boundary conditions on the surface of the scatterer as expressed by the extended boundary condition method. Translation and rotation of fields may also be achieved by linear transformations, and the relevant matrix elements are determined, respectively, by the translation-addition theorem and the rotation theorem for vector spherical wave functions (VSWFs), respectively. The details of both theorems may be found in Refs. 18 and 19. The final part of the calculation involves the evaluation of the forces and torques on a particle. Formally, this involves a surface integral of a vector-valued function of the Maxwell stress tensor.[10,20] The procedure for performing the calculations follows.

A. Vector Spherical Wave Function Expansion

The incident and scattered fields are written in terms of VSWFs in the following way:

$$\mathbf{E}^{\mathrm{inc}}(\mathbf{r}) = \sum_{n=1}^{\infty} \sum_{m=-n}^{n} [a_{mn}\mathrm{Rg}\mathbf{M}_{mn}(k\mathbf{r}) + b_{mn}\mathrm{Rg}\mathbf{N}_{mn}(k\mathbf{r})], \tag{2a}$$

$$\mathbf{E}^{\mathrm{sca}}(\mathbf{r}) = \sum_{n=1}^{\infty} \sum_{m=-n}^{n} [p_{mn}\mathbf{M}_{mn}(k\mathbf{r}) + q_{mn}\mathbf{N}_{mn}(k\mathbf{r})]. \tag{2b}$$

a_{mn}, b_{mn}, p_{mn}, and q_{mn} are a set of complex coefficients, which are to be determined. $\mathrm{Rg}\mathbf{M}_{mn}$, $\mathrm{Rg}\mathbf{N}_{mn}$, $\mathbf{M}_{mn}$, and $\mathbf{N}_{mn}$ are a complete set of VSWFs given previously,[4] k is the modulus of the wave vector in the background medium, and $\mathbf{r}$ is the relevant position vector. The summations in Eqs. (2a) and (2b) are truncated at a predetermined value of n (i.e., n max), which will depend on a convergence criterion (see below).

The first requirement in the scattering calculation is to obtain coefficients for the VSWF expansion of the incident field, which is taken to be a Gaussian beam. For reasons of accuracy, it is advisable to use one of the higher-order Davis beam approximations. In the following study, the fifth-order beam is used, coefficients for which may be found in the literature[20–22] and are reproduced in Appendix A for completeness.

B. T Matrix Description

Under the extended boundary condition method (EBCM), the T matrix for general particles is given by a set of integrals of vector cross products of vector spherical harmonics taken over the surface of the scatterer.[18] When the particle is spherical, this integral can be evaluated analytically resulting in a diagonal matrix, whose elements are given by the familiar Mie coefficients. For nonspherically symmetric particles, the integration must be performed numerically, although when there is rotational symmetry, the azimuthal part of the surface integral may be performed analytically leaving a one-dimensional integral that can be evaluated by quadrature.

Integrals for obtaining elements of the T matrices for spheroidal particles are given in Ref. 18. It should be noted that the integrands involved are oscillatory, so that

a sufficient number of points must be included in the quadrature to resolve the variation. The precise number of points necessary will depend on n max, the value of n for which the field expansions are truncated. A useful test of the computer code written to carry out the integration for spheroidal particles is to check that the analytical values for spherical particles are reproduced when the principal axes are equal. In the present case, it is found that, for n max<20, the quadrature achieves good agreement if approximately 10,000 or more points are used. For a code written in a compiled language, such as Fortran, the entire matrix may be evaluated in under a minute on a desktop computer, for n max$=20$.

C. Beam Transformations

The translation and rotation theorems[18] may be used to move the incident beam relative to the particle, so that the required position and orientation of the particle are achieved relative to the trap. When applying these theorems numerically, it should be noted that large translations will affect convergence.[4] In other words, the larger the distance over which the beam is translated, the greater the value of n max that will be required to achieve a desired level of accuracy (see below).

D. Scattered Field Calculation

The VSWF expansion of the scattered field was given above [Eq. (2b)]. The coefficients p_{mn} and q_{mn} are obtained by matrix multiplication of the T matrix by the transformed incident field coefficients, i.e.,

$$\tilde{p} = T \cdot \tilde{a}, \tag{3}$$

where $\tilde{a}$ is a vector consisting of an ordered set of the coefficients, a_{mn} and b_{mn}, from Eq. (2a) after suitable rotations and translations have been applied, and $\tilde{p}$ is an equivalent vector comprising the p_{mn} and q_{mn} coefficients. This step is most efficiently carried out by using an optimized matrix multiplication routine such as found in the LAPACK linear algebra package.[23]

E. Forces and Torques

The net force on a particle is found by integrating the product of the Maxwell stress tensor, $\underline{\underline{T}}_{\mathrm{M}}$, and the unit normal over a surface enclosing the particle[10,24]:

$$\mathbf{F} = \int_S \langle \underline{\underline{T}}_{\mathrm{M}}(\mathbf{r}) \rangle \cdot \mathrm{d}\mathbf{S}, \tag{4}$$

where

$$\langle \underline{\underline{T}}_{\mathrm{M}}(\mathbf{r}) \rangle = \frac{1}{2} \Re \left\{ \varepsilon \mathbf{E}(\mathbf{r}) \mathbf{E}^*(\mathbf{r}) + \mu \mathbf{H}(\mathbf{r}) \mathbf{H}^*(\mathbf{r}) - \frac{1}{2} [\varepsilon |\mathbf{E}(\mathbf{r})|^2 + \mu |\mathbf{H}(\mathbf{r})|^2] \underline{\underline{I}} \right\}. \tag{5}$$

$\mathbf{E}^*$ and $\mathbf{H}^*$ represent the complex conjugates of the electric and magnetic fields, and $\mathbf{E}\mathbf{E}^*$ is a dyadic product. The double underline indicates a second-rank tensor, angle brackets denote a time average for harmonic fields, and $\underline{\underline{I}}$ is the unit tensor. A similar technique is used for calculating torques:

$$\mathbf{\Gamma} = - \int_S r \mathrm{d}\mathbf{S} \cdot [\langle \underline{\underline{T}}_{\mathrm{M}}(\mathbf{r}) \rangle \times \hat{\mathbf{r}}]. \tag{6}$$

All of the fields involved in the above equations are total fields, and the material parameters are those of the medium in which the particle is immersed.

For single particles, the above integrals can be calculated in the far field, where they amount to a sum of products of the VSWF expansion coefficients, a_{mn}, b_{mn}, p_{mn}, and q_{mn}. Such equations have been developed for spheres by several authors.[8,20,25–27] In each case, the equations have structural similarities. Most conspicuously, if the coefficients in the scattered field expansion are zero, i.e., if there is no particle present, or if the refractive index of the particle is identical to that of the background medium, the calculated forces and torques will also be zero as should be the case. This essential property is replicated by the numerical integration used throughout this paper.

The equations most easily adapted to our purposes are those due to Barton *et al.*[8] The basis functions used by Barton *et al.* are normalized differently from those used here; accounting for the differences in normalization leads to the following equations connecting the two sets of expansion coefficients (the dashed coefficients are from Ref. 8):

$$a'_{mn} = \frac{-ia_{mn}n_m}{k^2A^2[n(n+1)]^{1/2}}, \quad p'_{mn} = \frac{-ip_{mn}n_m}{k^2A^2[n(n+1)]^{1/2}},$$

$$b'_{mn} = \frac{b_{mn}}{k^2A^2[n(n+1)]^{1/2}}, \quad q'_{mn} = \frac{q_{mn}}{k^2A^2[n(n+1)]^{1/2}}, \tag{7}$$

where A is a size parameter for the sphere in the derivation of Barton *et al.*, and n_m is the refractive index of the medium. Substitution of the above relationships into Eqs. (10)–(12) of Ref. 8 gives a set of expressions for the torque, which are generally applicable to *any* shape of the particle:

$$\Gamma_x = \frac{-E_0^2 \epsilon_m}{8\pi k^3} \sum_{n=1}^{\infty} \sum_{m=-n}^{n} \Re \left\{ \sqrt{(n-m)(n+m+1)} \times \left[q_{mn} q^*_{m+1,n} + p_{mn} p^*_{m+1,n} + \frac{1}{2} (q_{mn} b^*_{m+1,n} + q_{m+1,n} b^*_{mn} + p_{mn} a^*_{m+1,n} + p_{m+1,n} a^*_{mn}) \right] \right\}, \tag{8a}$$

$$\Gamma_y = \frac{-E_0^2 \epsilon_m}{8\pi k^3} \sum_{n=1}^{\infty} \sum_{m=-n}^{n} \Im \left\{ \sqrt{(n-m)(n+m+1)} \times \left[q_{mn} q^*_{m+1,n} + p_{mn} p^*_{m+1,n} + \frac{1}{2} (q_{mn} b^*_{m+1,n} - q_{m+1,n} b^*_{mn} + p_{mn} a^*_{m+1,n} - p_{m+1,n} a^*_{mn}) \right] \right\}, \tag{8b}$$

$$\Gamma_z = \frac{-E_0^2 \epsilon_m}{8\pi k^3} \sum_{n=1}^{\infty} \sum_{m=-n}^{n} m[|q_{mn}|^2 + |p_{mn}|^2 + \Re(p_{mn} a_{mn}^* + q_{mn} b_{mn}^*)]. \quad (8c)$$

E_0 is the magnitude of the electric field at the beam focal point, and ε_m is the permittivity of the ambient medium; the asterisks denote complex conjugates.

In the work presented in Section 3, the integrals were performed both numerically and analytically. For the torque calculations, precise correspondence was found between the results of numerical integration and Eqs. (8a)–(8c). For the force calculations, it was found similarly that numerical integration of Eq. (4) produced agreement with the expressions derived by Moine and Stout[20] and also with force expressions (not shown) following from the work of Barton *et al.*[8]

F. Convergence

Before continuing, it is worth emphasizing a further point concerning convergence. As mentioned above, the translation of incident fields has a deleterious effect on convergence, such that a higher value of n max is generally required. Fortunately, no such effect is noticeable when the incident fields are rotated. However, increasing the aspect ratio of the particles causes further problems with the convergence. The underlying causes of this have been analyzed by a number of authors.[28–30] In essence, the problems stem from the use of spherical harmonic expansions in scattering problems involving nonspherical symmetry, which inevitably requires the use of high-order terms.

Figure 1 gives some quantitative insight into the issues concerning convergence encountered in this work. Values of the fractional change in calculated force with increasing n max are given for a variety of silica glass ellipsoids ($n_m = 1.45$) displaced by 0.6 μm below the focal point of the beam. In all calculations, the background medium is

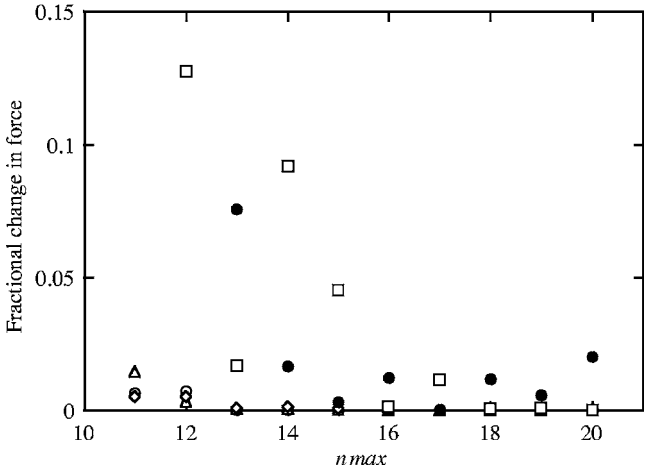

Fig. 1. Convergence characteristics for force calculations of single silica particles in Gaussian beams: spherical particles with $\rho = 1$ μm (open circles) and 2 μm (triangles); prolate spheroids with $\delta = 2$ and $\rho_e = 1$ μm and the long axis parallel to the x axis (diamonds) or the z axis (squares); prolate spheroids with $\delta = 2$ and $\rho_e = 2$ μm and the long axis parallel to the z axis (solid circles). In each case, the particles are displaced below the focus by 0.6 μm with the beam incident from above.

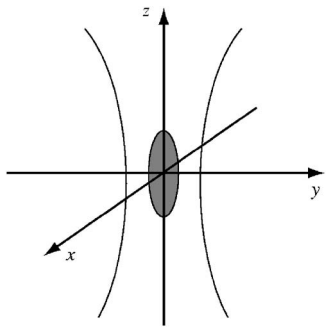

Fig. 2. Gaussian beam geometry. Light is incident from above traveling in the negative z direction and polarized parallel to the x axis. A prolate spheroid with a major axis parallel to z is shown.

taken to be water ($n_m = 1.33$), the frequency of the incident radiation is 3.75×10^{14} Hz, which corresponds to a wavelength of 600 nm in water, and the radius of the beam waist is 0.3 μm. Data are presented for spheres with a radius of $\rho = 1$ μm (open circles) and 2 μm (triangles), prolate spheroids with an aspect ratio of $\delta = 2$, and an equivalent radius of $\rho_e = 1$ μm with the symmetry axis aligned parallel to the x axis (diamonds) and the z axis (squares) and larger ellipsoids with $\delta = 2$ and $\rho_e = 2$ μm aligned parallel to the z axis (solid circles). The geometry is illustrated in Fig. 2. The equivalent radius is defined in such a way that a spheroid with $\rho_e = 1$ μm has the same volume as a sphere with $\rho = 1$ μm.

As previously,[4] we take the criterion for convergence as

$$\left| \frac{|F^i| - |F^{i-1}|}{|F^{i-1}|} \right| \leq 0.001, \quad (9)$$

where $|F^i|$ is the modulus of the force calculated for n max$=i$. For the spherical particles, it can be seen that convergence is achieved for n max≥ 13. The rate of convergence is poorer for anisotropic particles, especially when they present their smallest profile to the incoming beam. For example, force calculations on prolate spheroids with $\rho_e = 1$ μm oriented parallel to the z or beam axis converge for n max≥ 18; whereas similar particles with an equivalent radius of 2 μm fail to converge over the range of n max studied. Taking these considerations into account, attention will be focused, in this paper, on spheriods with aspect ratios in the range of $0.5 \leq \delta \leq 2.0$ and with a maximum volume equivalent to that of a sphere of a 1 μm radius. Under these conditions, convergence is reliable and all calculations can be performed with n max $= 18$.

3. RESULTS

An equilibrium configuration of an arbitrary particle can be defined as any position and orientation for which all the forces and torques on the particle vanish and can therefore be specified by three positional and three orientational coordinates. When the forces are those associated with an external field of some sort, sufficient conditions for equilibrium can be stated in terms of the symmetry of the system, i.e., of the fields and particles. For example, if the system contains a mirror plane, then the force perpendicular to this plane must be zero. Similarly, the torque

about any axis contained within a mirror plane must also be zero. Since a laser beam does not have a plane of symmetry perpendicular to its axis, positional equilibrium in this direction does not result from symmetry requirements but can be seen, for example, as arising from a balancing of radiation pressure and gradient forces. Hence, in general, symmetry conditions are sufficient, but not necessary, for determining equilibrium configurations.

If the beam is linearly polarized, then, in terms of its interaction with a dielectric particle, it effectively contains two mirror planes through its axis, one containing the polarization vector of the electric field, the second orthogonal to the first. If the particle is similarly symmetric, then there must be equilibrium positions that lie on the beam axis. With these considerations in mind, it can be seen that a spheroidal particle will have at least three equilibrium configurations, each one corresponding to one of the permissible orientations of the principal axes with respect to the beam and polarization directions and each having an equilibrium position at a different point along the beam axis.

For these configurations to trap the particle, the equilibrium must be stable with respect to both translation and rotation. In the following sections, equilibrium configurations for spheroidal particles are calculated, and their stability is analyzed by examining the effect of small displacements and rotations on the forces and torques felt by each particle. Figure 2 shows the coordinate system that is being used. The incident beam is directed down the z axis and has a focal point at the origin; it is polarized parallel to the x axis. The translational stability of the equilibrium position to small perturbations parallel to z is indicated by the sign of the translational stiffness parameter given by

$$K^t_{z\beta} = \frac{\partial Q_{F,z}}{\partial z}, \tag{10}$$

where $Q_{F,z}$ is the z component of the trapping efficiency for a particle aligned along axis β defined for the *force*, F_z, by

$$Q_{F,z} = \frac{F_z c}{n_m P}. \tag{11}$$

c is the speed of light *in vacuo*, n_m is the refractive index of the background medium, and P is the power in the beam. A negative value of the stiffness parameter implies a force directed back, toward the equilibrium position.

The rotational stability of a uniaxial particle is examined by reference to two similar parameters, each quantifying the change in torque experienced by the particle as it undergoes infinitesimal rotations from the equilibrium orientation about each of the axes perpendicular to its symmetry axis. For example, the rotations relevant to the ellipsoid drawn in Fig. 2 are about the x and y axes. The rotational stiffness parameters are given by

$$K^r_{\alpha\beta} = \frac{\partial Q_{T,\alpha}}{\partial \theta_\alpha}, \tag{12}$$

where the symmetry axis of the spheroid is aligned with axis β, and rotations are about axis α. α and β refer to the coordinate axes, x, y, and z. $Q_{T,\alpha}$ is a trapping efficiency defined for the *torque* T_α about axis α; θ_α is the angle through which the particle is rotated about that axis. We define the torque trapping efficiency in a similar way to the *force* trapping efficiency:

$$Q_{T,\alpha} = \frac{T_\alpha c}{n_m P \lambda}, \tag{13}$$

where λ is the wavelength of the incident beam in the surrounding medium. As with the force trapping efficiency, this expression is dimensionless, and also has the advantage that, unlike some definitions in the literature, it gives zero in the absence of a particle or if the particle has the same refractive index as the medium. The derivatives in Eq. (12) are taken such that a positive θ_α corresponds to a clockwise rotation about the named axis. As in the case of translations, rotational stability is indicated by negative values of the stiffness parameters.

The stiffness parameters discussed above quantify the changes in force, or torque, associated with small displacements about the equilibrium configurations. However, it is sometimes more informative to consider changes in directly observable quantities. For particles of the sizes considered here, immersed in water, typical values for Reynolds numbers are in the vicinity of 10^{-4}. In this regime, terminal velocities (angular or linear) are reached virtually instantaneously. The forces are then related to velocities and torques to rotational velocities by the translational and rotational friction tensors, respectively. Specifically,

$$\mathbf{F} = \underline{\underline{\mathbf{f}}}^t \cdot \mathbf{v}, \tag{14a}$$

$$\mathbf{T} = \underline{\underline{\mathbf{f}}}^r \cdot \boldsymbol{\omega}, \tag{14b}$$

where $\mathbf{F}$ is the force; $\mathbf{T}$ is the torque; $\underline{\underline{\mathbf{f}}}^r$ and $\underline{\underline{\mathbf{f}}}^t$ refer to the rotational and translational friction tensors, respectively; and $\mathbf{v}$ and $\boldsymbol{\omega}$ are the linear and angular velocities. Since attention is being focused here on uniaxial particles, these tensors have one eigenvalue expressing the frictional forces felt when the spheroids are rotated about their symmetry axes and a further two identical eigenvalues relating to rotations about the perpendicular axes. Since symmetry prevents optical forces from imposing torques about the unique axis of the particle, only the perpendicular eigenvalues are of interest.

Values for these elements of the rotational friction tensor may be obtained by evaluating[31]

$$f^r_{\mathrm{perp}} = \frac{16\pi\eta}{3}\left[\frac{a^2+b^2}{\alpha_a a^2 + \alpha_b b^2}\right], \tag{15}$$

in which

$$\alpha_a = \int_0^\infty \frac{\mathrm{d}\lambda}{(a^2+\lambda)^{3/2}(b^2+\lambda)}, \tag{16}$$

$$\alpha_b = \int_0^\infty \frac{d\lambda}{(a^2+\lambda)(b^2+\lambda)^{3/2}}. \quad (17)$$

a and b are the primary and secondary radii of the spheroid (as defined above), and η is the viscosity of the surrounding fluid.

As might be anticipated, both from physical intuition and from the appearance of the values of the radii in the denominators of α_a and α_b, the value of the perpendicular element of the friction tensor increases rapidly with equivalent radius; i.e., the larger the particle, the greater the resistance to motion. Representative values of the rotational friction coefficient, f^r_{perp}, are given in Fig. 3 for spheroids of varying aspect ratios. It can be seen to vary over 4 orders of magnitude as the equivalent radius changes by a factor of 10. Since the angular velocity relating to an applied torque is given by dividing by f^r_{perp}, it can be seen that there will be a corresponding decrease in angular velocity with an equivalent radius.

In combination with Eqs. (11) and (13), Eqs. (14a) and (14b) provide a sensitive method of quantifying the trap stiffnesses in terms of angular and translational velocities. Thus, by analogy with Eq. (12), we may define an angular velocity gradient as

$$G_{\alpha\beta} = \frac{\partial \omega_\alpha}{\partial \theta_\alpha}. \quad (18)$$

This gives a more sensitive indication of the susceptibility of a particle to motion under an applied torque and of how rapidly a displaced particle will recover its equilibrium configuration than quantities defined in terms of the torque alone.

A. Prolate Spheroids

Figure 4 shows maps of the trapping positions of prolate spheroids oriented in each of the three orthogonal, torque-free directions. The positions are measured with respect to an origin at the focus of the beam. The vertical axis represents the aspect ratio of the ellipsoids δ, while the horizontal axis is the equivalent radius ρ_e, i.e., the radius of a sphere of equivalent volume to the ellipsoid. Graphs showing the trapping positions of spheres, and spheroids with $\delta=2$, have been extracted and plotted in Fig. 5. When the symmetry axes of the spheroids are perpendicular to the beam axis, the variation of trapping position with the equivalent radius is oscillatory, as might be expected from knowledge of the Mie theory and similar to

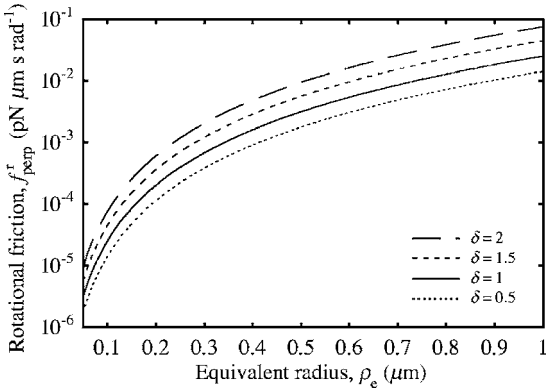

Fig. 3. Perpendicular component of the rotational friction tensor f^r_{perp} as a function of equivalent radius for spheroids with a range of aspect ratios.

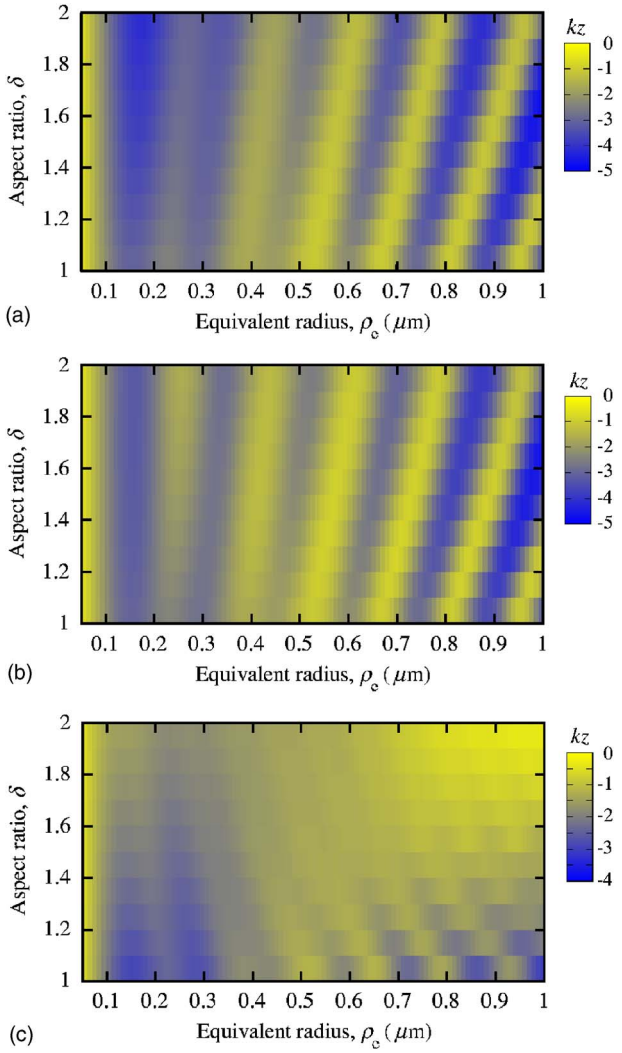

Fig. 4. (Color online) Maps showing the equilibrium trapping position, in dimensionless units kz, for prolate spheroidal silica particles with aspect ratios $\delta \leq 2$ and equivalent radii $\rho_e \leq 1$ μm with the symmetry axis of the particle aligned parallel to (a) x, (b) y, and (c) z axes.

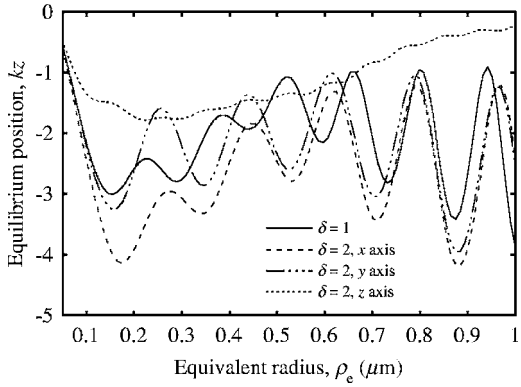

Fig. 5. Line plots extracted from Fig. 4 showing the equilibrium trapping position as a function of equivalent radius ρ_e for spheres ($\delta=1$) and prolate spheroids with $\delta=2$ oriented with symmetry axis parallel to each of the coordinate axes.

the trapping behavior of a sphere. The period of the oscillations increases with the increasing aspect ratio. In fact, the period increases approximately in proportion with the cube root of the aspect ratio. In other words, the periods may be brought into line approximately by plotting the data against a minor radius instead of the equivalent radius. The minor differences that may be observed between Figs. 4(a) and 4(b) arise because the beam is polarized in the x–z plane.

The equilibrium positions for spheroids, whose symmetry axis is parallel to the beam, are radically different from those of the orthogonal orientations. This distinction has a simple explanation in terms of the concepts discussed in Section 1. The shape of the focal region of the Gaussian beam is elongated along the z axis (see Fig. 2). Vertically aligned prolate spheroids are able to overlap this intensity distribution more effectively than horizontal ones. In addition, the vertically aligned particles present a smaller cross section to the incoming beam thus diminishing the effect of downward radiation pressure. The reduction in downward radiation pressure combined with the increased energetic advantage of overlapping the focus more fully means that the vertically aligned particles tend to sit higher in the beam than do the horizontal particles. Evidently, this effect is enhanced as the volume of the particle is increased.

Figure 6 shows the translational stiffness, $K^t_{z\beta}$, for prolate spheroids with $\delta=2$ in each of the orthogonal orientations and for spheres. The stiffness is evaluated for small displacements from the equilibrium position. In each case, it is negative, indicating that the trap is stable with respect to translational perturbation and, beyond a certain point related to the diameter of the beam, tends to diminish in magnitude with increasing particle size. There are no significant changes in similar plots for spheroids with lower aspect ratios.

The measures of rotational stiffness are more interesting. Figure 7 shows the rotational stiffness parameters, $K^r_{\alpha\beta}$, relevant to each of the three distinct equilibrium orientations for prolate spheroids with $\delta=2$, the components being indicated in the figure. For the moment, results for small spheroids are ignored—they are not discernible in the main figure. Figure 7(a) shows that the configuration with the particle aligned with the symmetry axis parallel to the polarization vector is generally stable with respect

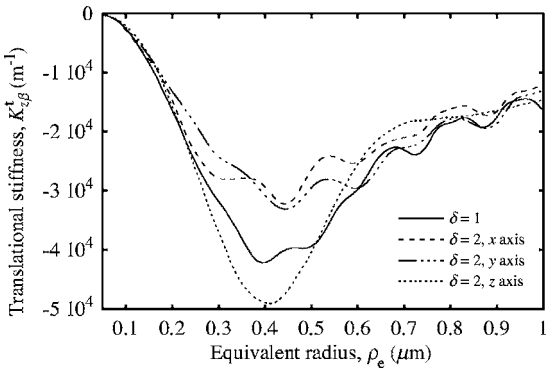

Fig. 6. Translational stiffness, $K^t_{z\beta}$, for spheres and prolate spheroids of silica with $\delta=2$ oriented parallel to each of the coordinate axes.

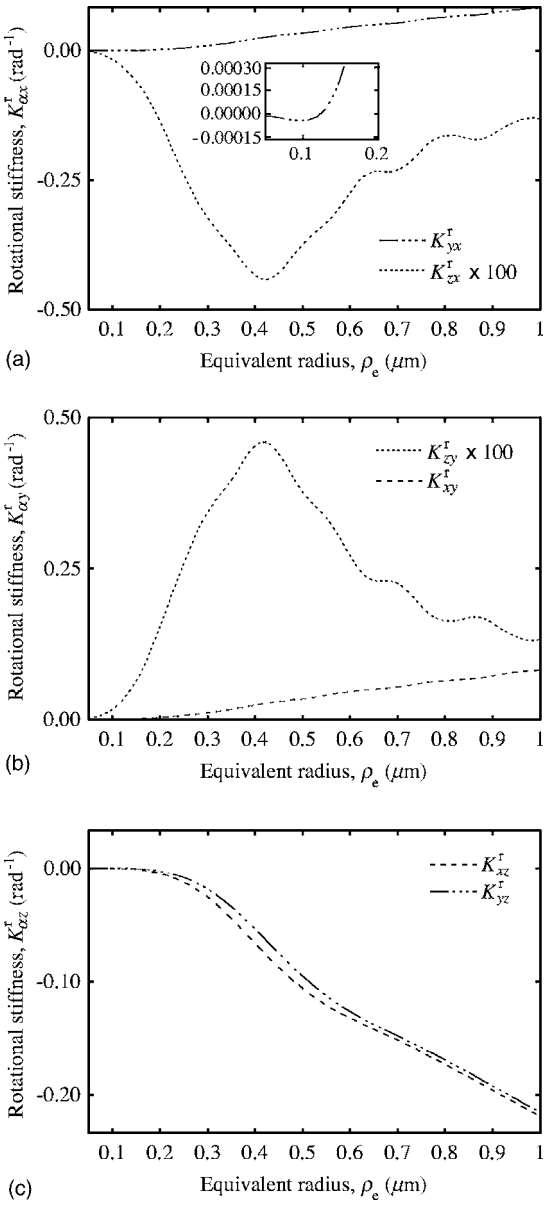

Fig. 7. Rotational stiffness parameters, $K^r_{\alpha\beta}$, for prolate silica spheroids with $\delta=2$ aligned with the symmetry axis parallel to (a) x, (b) y, and (c) z axes. For each alignment, parameters are shown for rotations about each of the other two axes.

to rotations about the beam axis but apparently unstable with respect to rotation about the y axis. In other words, equilibrium points for this orientation are saddle points: small fluctuations are likely to result in a reorientation toward the vertical, but in the x–y plane, there is a preference for alignment with the polarization vector. In Fig. 7(b), the configuration with the symmetry axis perpendicular to both the beam axis and the polarization vector is shown to be unstable with respect to both relevant rotations, while alignment of the symmetry axis with the beam axis leads to stability in all respects [Fig. 7(c)]. All of these findings are in accordance with physical intuition. There are energetic reasons why the particle will try to maximize its overlap with the intensity distribution, and if it is constrained from doing this, it will reorient itself parallel to the polarization vector of the electric field.

At smaller volumes, however, the situation is slightly different. This is apparent in the inset to Fig. 7(a); in which there appears to be a slight restoring force toward the x–y plane for rotations about the y axis. The effect is seen more clearly in Fig. 8, in which the angular velocity gradients, $G_{\alpha\beta}$, have been plotted for the same rotations as shown in Fig. 7. For small spheroids ($\rho_e < 0.122\ \mu$m), Fig. 8(a) shows that the configuration with the symmetry axis aligned parallel to the polarization vector is stable. Conversely, Fig. 8(c), showing the results for the vertically oriented spheroids indicates that this configuration is unstable for small ellipsoids against rotations about the y axis. Combining these observations demonstrates that, for sufficiently small spheroids, the preferred orientation is parallel to the polarization vector. This behavior can be qualitatively explained by realizing that, for small spheroids, the variation in intensity across the length of the particle becomes negligible, and the impact of orientation on the overlap with the intensity profile is reduced. Consequently, the advantages to alignment with the polarization vector become relatively more significant, and below a certain threshold, this configuration will be selected. Figure 9 shows how this transition point varies with the aspect ratio. As might be predicted, the lower the aspect ratio, the broader the range of equivalent radii over which the horizontal orientation is stable, but this is associated with a weakening of the restoring torques.

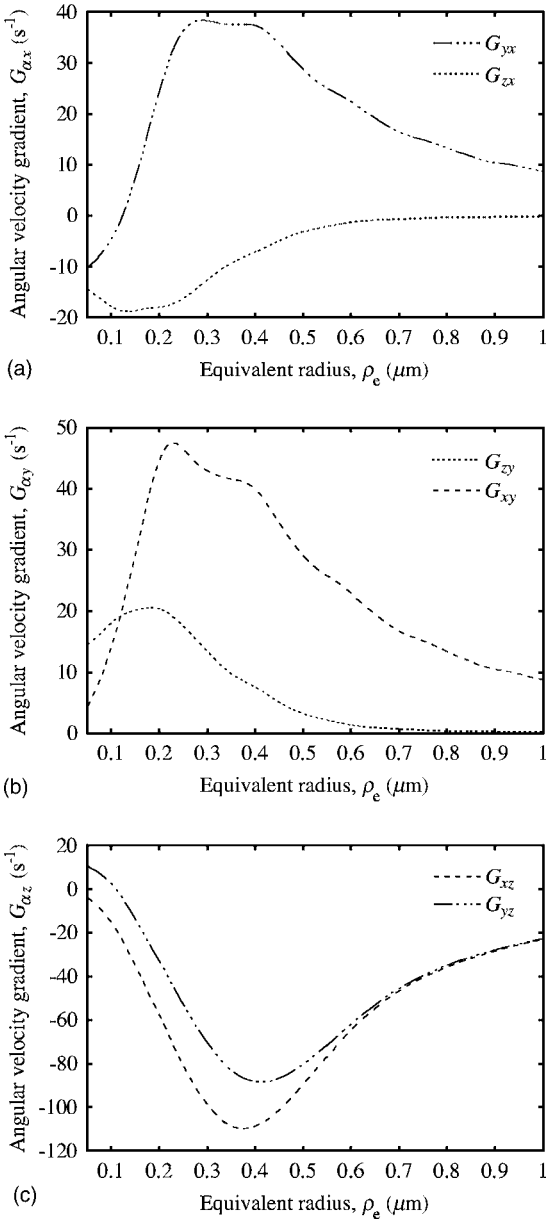

Fig. 8. Rotational velocity gradients, $G_{\alpha\beta}$, for prolate silica spheroids with $\delta = 2$ aligned with the symmetry axis parallel to (a) x, (b) y, and (c) z axes. As with Fig. 7, parameters are shown for each alignment for rotations about each of the remaining axes.

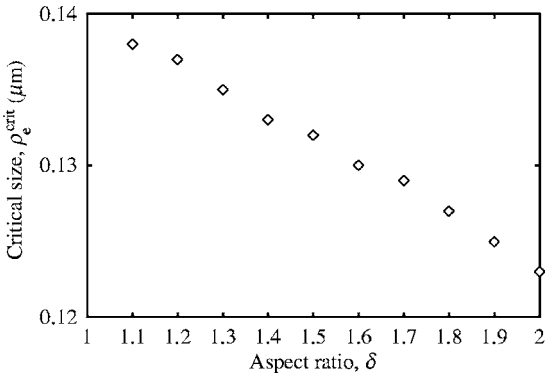

Fig. 9. Critical value of particle size, as given by the equivalent radius, ρ_e^{crit}, at which the transition occurs between stable orientation of the prolate spheroid parallel to the polarization vector (small particles) and stable orientation parallel to the beam (large particles).

B. Oblate Spheroids

The trapping behavior of oblate spheroids is qualitatively different from that of the prolate variety. However, the same principles can be seen to be active. Accordingly, the particles seek to maximize their overlap with the intensity profile of the beam while simultaneously aligning themselves in some way with the polarization vector of the electric field. Unlike prolate spheroids, oblate spheroids can satisfy both of these requirements at the same time. In a static field, an oblate dielectric spheroid has a uniaxial polarizability tensor, whose eigenvalues are greater for vectors perpendicular to the symmetry axis than they are for vectors parallel to it. In other words, the symmetry axis is the *short* axis, and perpendicular axes may be described as *long* axes. It is possible, therefore, to align a direction of higher polarizability with the electric field while maximizing the overlap with the intensity profile by orienting the symmetry axis perpendicular to both the electric polarization vector and the beam axis. It is found that this is the stable configuration for oblate spheroids of any volume within the range considered here. This trapping orientation has been reported for spinach chloroplasts (*Spinacia oleracea*), which crudely resemble oblate spheroids.[5]

Figure 10 shows the equilibrium trapping positions for spheroids aligned in the manner described above. The variation of trapping position with equivalent radius is again oscillatory, but this time, increasing the anisotropy, i.e., decreasing the aspect ratio, appears to reduce the amplitude of the regular oscillations. Reducing the aspect ratio also reduces the period of the oscillations continuing

the trend established for prolate spheroids. The stability of these configurations is demonstrated in Fig. 11 where the translational stiffness $K^t_{z\beta}$ [Fig. 11(a)], rotational stiffness $K^r_{\alpha y}$ [Fig. 11(b)], and angular velocity gradients $G_{\alpha y}$ [Fig. 11(c)] are plotted for spheroids with aspect ratios of 0.5. As might be expected, the angular stiffness of these traps is significantly greater for rotations that take the symmetry axis toward the beam axis, thus decreasing the overlap with the intensity profile, than it is for rotations that move the symmetry axis toward the polarization direction. It would appear that the effect of anisotropy in the intensity profile on the orientation is substantially greater than the effect of the polarization direction. It is worth noting that the orthogonal orientation with a symmetry axis parallel to the polarization vector (not shown here) is unstable to perturbations about the beam axis.

The feature that makes the trapping of oblate spheroids distinct from prolate ones is that the oblate spheroids align with their symmetry axes perpendicular to the beam axis, while prolate spheroids generally adopt the parallel alignment (with the exception of the smallest particles noted above). This leads to the existence of restoring torques for rotations of the oblate spheroids about the beam axis. Their presence can be inferred by the rotational stiffness data plotted in Fig. 11(b), but is demonstrated explicitly in Fig. 12(a) in which the variation of torque is plotted as a function of the angular deviation from the polarization vector for a spheroid with ρ_e

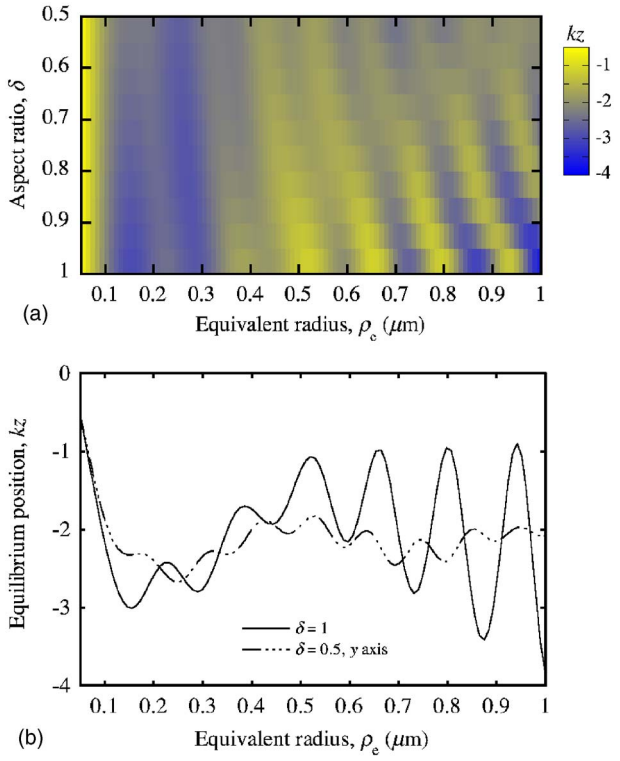

Fig. 10. (Color online) (a) Trapping position, expressed as the dimensionless parameter kz, of oblate silica spheroids oriented with the symmetry axis parallel to the y axis and secondary (major) axes parallel to the polarization vector (x axis) and beam axis as a function of the aspect ratio and equivalent radius. (b) Line plots extracted from (a) for spheres and oblate spheroids with δ=0.5.

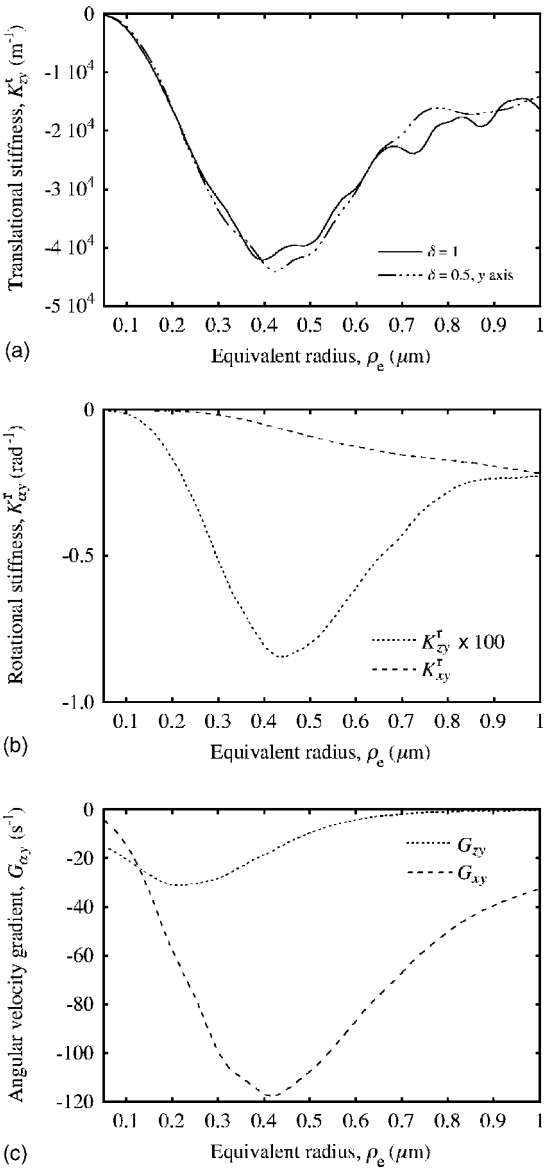

Fig. 11. (a) Translational stiffness parameter parallel to the beam axis, K^t_{zy}, for spheres and oblate spheroids of silica with δ =0.5 oriented with the symmetry axis parallel to the y axis and secondary axes parallel to the polarization vector (x axis) and the beam axis as a function of equivalent radius. (b) Rotational stiffness parameters, $K^r_{\alpha y}$, for the same oblate spheroid as in (a) for rotations about the x and z axes. (c) Similar plots of the angular velocity gradients $G_{\alpha y}$.

=0.5 μm and δ=0.5. As can be seen, the variation of torque with an angle is sinusoidal; in fact, the torque is proportional to $\sin 2\phi$ where ϕ is the angle between the beam polarization vector and the long axis of the spheroid, which is exactly the result expected for a point polarizability in such a field. That the torque is negative implies that any particle not aligned with its long axis parallel to the polarization direction will rotate backward until it is. The only exception will be particles sitting at 90° to the polarization vector, which will not move until Brownian motion nudges them out of unstable equilibrium. Changes in the setting angle are accompanied by changes in the component of the force parallel to the beam axis [Fig. 12(b)]. This is a consequence of the fact

that the equilibrium positions of oblate spheroids in the trapping beam are dependent on the orientation of the particle just as they were for the prolate spheroids.

The variation of torque with angle leads to a propensity for the particle to rotate with the plane of polarization. The equation of motion for such a particle in the low Reynolds number regime exposed to a continuously varying plane of polarization is given by[12]

$$f^r_{\mathrm{perp}}\dot{\theta} = T_z \sin[2(\Omega t - \theta)], \tag{19}$$

where Ω is the angular velocity of the plane of polarization. For sufficiently large values of T_z or sufficiently small values of Ω, this equation has steady-state solutions:

$$\theta = \Omega t - \phi, \tag{20}$$

where ϕ now represents a constant offset between the polarization vector and the long axis of the particle in the x–y plane. It follows from Eqs. (19) and (20) that ϕ is given by

$$\sin\phi = \frac{f^r_{\mathrm{perp}}\Omega}{T_z}, \tag{21}$$

and that there will be a maximum value of Ω given by

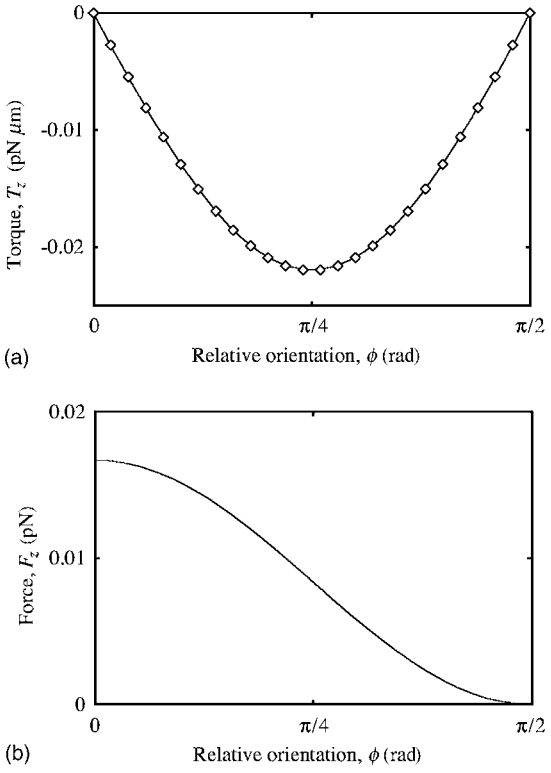

Fig. 12. (a) Torque, T_z, induced by a 1 mW beam on an oblate silica spheroid with $\rho_e = 0.5\ \mu$m, and $\delta = 0.5$. The particle lies with its symmetry axis in the x–y plane and an angle ϕ between the long axis of the spheroid and the polarization vector. The solid curve shows the calculated values; the diamonds indicate a sine curve, suitably scaled, for comparison. The height of the particle in the beam corresponds to the equilibrium position when the particle is held with the symmetry axis parallel to the polarization vector, i.e., $\phi = \pi/2$. (b) z component of force on the particle as ϕ varies.

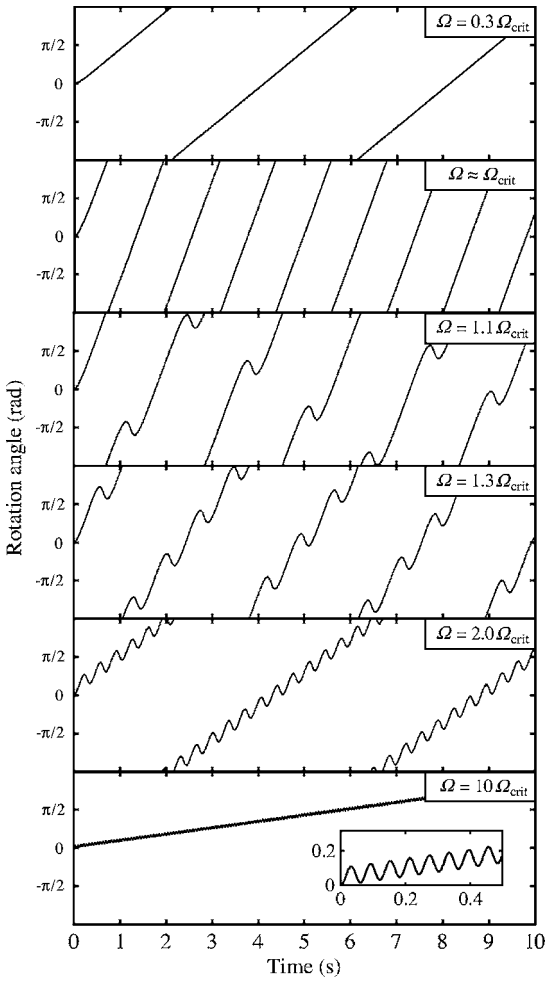

Fig. 13. Rotation of an oblate silica spheroid, $\rho_e = 0.5\ \mu$m, $\delta = 0.5$, induced by a rotating polarization vector with frequency Ω. The spheroid is oriented with its symmetry axis in the x–y plane.

$$\Omega_{\mathrm{crit}} = \frac{T_z}{f^r_{\mathrm{perp}}} \tag{22}$$

corresponding to $\phi = 90°$ and beyond which the steady-state solution breaks down.

Figure 13 shows solutions of Eq. (19) obtained by numerical integration for an oblate particle ($\delta = 0.5$) for several values of Ω. In this case, $\Omega_{\mathrm{crit}} \simeq 5.2$ rad/s, and as the frequency of rotation of the polarization plane is increased, the rate of rotation of the particle increases until this value is reached. Beyond this point, the motion acquires an oscillatory component superposed on top of the steady rotation, a consequence of the particle intermittently failing to keep up with the changing polarization. Increasing Ω further results in a gradual reduction in both the amplitude of the oscillation and the rate of rotation of the particle. In the high-frequency limit, any response of the particle to the changing polarization will likely be masked by Brownian fluctuations.

C. Circularly Polarized Light

In the situation described above, the transfer of angular momentum to the particle occurs as a consequence of the motion of the particle itself. If the particle were held sta-

tionary, it would feel a sinusoidally varying torque that averaged to zero over an integer number of periods and that, indeed, is what is observed in the high-frequency limit of Eq. (19). It is interesting, therefore, to consider the behavior of the particle in a circularly polarized beam. This situation is, however, subtly different from the rotating polarization described above. As has been discussed elsewhere, a circularly polarized *plane wave* carries no angular momentum.[32] It will, however, induce torques on a variety of particles, from the quartz wave plates of Beth[33] to absorbing particles[25,34] or particles having anisotropic refractive indices.[35] Circularly polarized beams have also been observed to impart angular momentum to trapped particles having either geometric or optical anisotropy. This behavior has been the subject of some controversy, the resolution of which has been attributed to the boundary conditions on the material or, in the case of beams, to edge effects.[25] It will be discussed in Section 4.

It is a straightforward matter to incorporate circular polarization in the T matrix method, in which case, forces and torques may be evaluated as before. Here, we examine, specifically, the case of oblate silica spheroids, oriented as above, with the symmetry axis in the x–y plane. Figure 14 shows the trapping positions for such spheroids with $\delta=0.5$ in circularly polarized light as compared with the linear polarization parallel and perpendicular to the symmetry axis of the spheroid. In the presence of the circularly polarized beam, it may be seen that the trapping positions are approximately midway between the equilibrium positions for the two linear polarizations of beam as might have been expected.

The torques experienced by these particles have also been calculated, and the rotation frequencies have been determined for 1 mW beams using Eq. (14b). The results are shown in Fig. 15. According to these calculations, the torque experienced by these particles is approximately one tenth of that corresponding to the maximum values associated with linearly polarized beams. The values obtained for spheres are negligible as they should be. However, the most intriguing aspect of the results shown in Fig. 15 is that, while for very small and large particles, the rotation is in the same sense as the angular momentum of the beam (negative in this case), there is a region of the plot, for intermediate particle sizes, in which the sense of rotation is *opposite* to the sense of angular momentum of the beam completely counter to what might normally be expected.

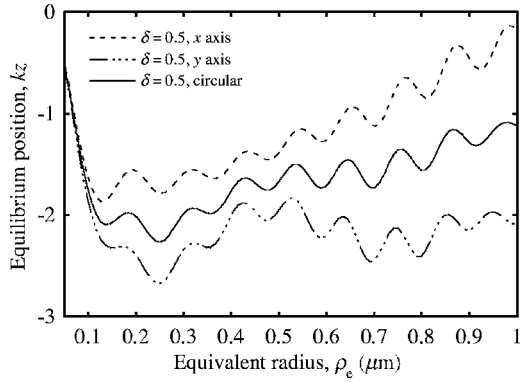

Fig. 14. Trapping position expressed as the dimensionless parameter kz of an oblate silica spheroid oriented with its symmetry axis in the x–y plane. The plot compares the effect of a circularly polarized beam with the linear polarization aligned parallel (x axis) and perpendicular (y axis) to the symmetry axis of the particle.

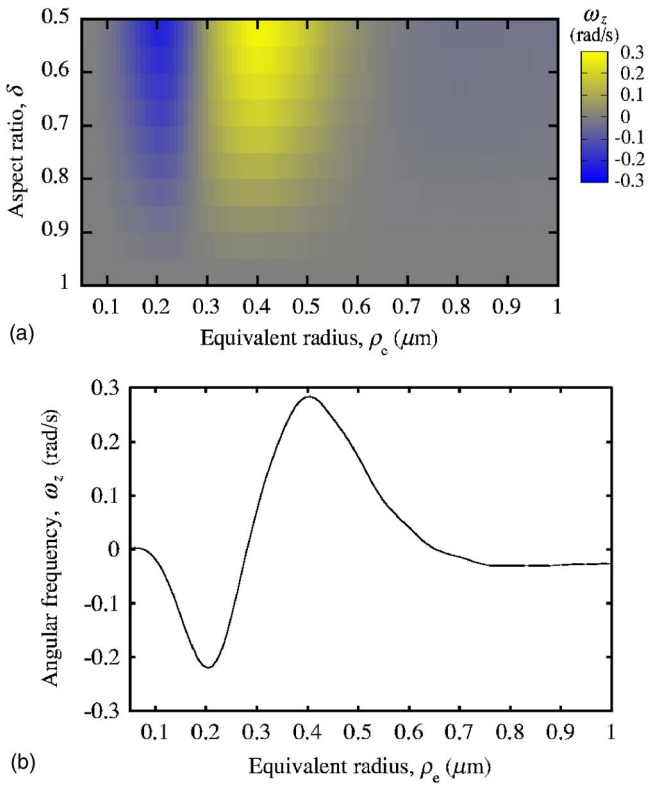

Fig. 15. (Color online) Frequency of rotation of oblate silica particles trapped in a 1 mW circularly polarized Gaussian beam. The particles are oriented with their symmetry axes in the x–y plane. (a) Map showing the frequency as a function of aspect ratio δ and equivalent radius ρ_e. (b) Single plot taken from (a) $\delta=0.5$.

The unusual nature of the results shown in Fig. 15 made it important to attempt some independent verification of the predictions. This was achieved in two ways: first by evaluating the torques analytically using the expressions in Eqs. (8a)–(8c) and second, by using finite-difference time-domain (FDTD) calculations. In the case of the analytical calculations, the agreement was essentially exact provided that n max was sufficiently large. Very minor deviations were observed using the FDTD approach, which could be attributed to the discrete nature of the lattice used. The FDTD results will be reported elsewhere.[36]

4. DISCUSSION

The calculations presented above have demonstrated that the trapping of spheroids can be qualitatively thought of in terms of a propensity for the particles to overlap the intensity distribution of the incident field and, where possible, align themselves with the plane of polarization, each in the presence of a prevailing downward radiation pressure. Small prolate spheroids therefore tend to preferentially align themselves with the polarization direction, while larger particles align themselves with the

beam axis. The transition between these equilibrium orientations has been seen to be dependent on the volume and the aspect ratio of the spheroids. Oblate spheroids behave differently, having only one equilibrium orientation that satisfies both of the previously mentioned conditions. In this configuration, oblate particles are sensitive to the plane of polarization and will seek to align themselves to it, enabling them to be rotated as desired. Unexpected behavior is observed in the presence of circularly polarized beams in which oblate spheroids of certain sizes acquire angular momenta in the opposite direction to that which would be expected from a consideration of the angular momentum of the beam.

Many of these phenomena, with the exception of the last mentioned, have been observed experimentally in systems that approximate to the ones considered here. As mentioned in Section 1, the flat particles studied by Galajda and Ormos[13] and the chloroplasts of Bayoudh *et al.*[5] have been observed to behave similarly to the oblate ellipsoids studied here. The vertical equilibrium orientation of elongated particles has been observed by several people (see, for example, Refs. 11 and 12); the horizontal alignment of very small particles accords with physical intuition although direct observation may be complicated by the size of the particles in question.

The unusual rotational behavior of oblate spheroids in circularly polarized beams remains more elusive and deserves some discussion. An instinctive reaction to this behavior would be that it infringes the requirement that angular momentum be conserved, and that the calculations must be flawed in some way; the beam has angular momentum in one sense but imparts it in the opposite sense. A more nuanced view can be arrived at by considering the underlying mechanisms in more depth. Barnett[37] has developed a mathematical framework for understanding the transport of linear and angular electromagnetic momentum. Within this framework, linear and angular momentum can be thought of as examples of conserved quantities like energy. They therefore have associated with them densities from which they derive by way of volume integrals, i.e., following Barnett:

$$\mathbf{j} = \mathbf{D} \times \mathbf{B}, \tag{23a}$$

$$\mathbf{l} = \mathbf{r} \times \mathbf{D} \times \mathbf{B}, \tag{23b}$$

where $\mathbf{j}$ is the electromagnetic momentum density, and $\mathbf{l}$ is its angular counterpart. These densities obey continuity relationships that express the conservation of the quantity in question:

$$\frac{\partial j_i}{\partial t} + \frac{\partial T_{\mathrm{M},ij}}{\partial x_j} = 0, \tag{24a}$$

$$\frac{\partial l_i}{\partial t} - \frac{\partial M_{ij}}{\partial x_j} = 0. \tag{24b}$$

$\underline{\underline{T}}_{\mathrm{M}}$ is the Maxwell stress tensor from Eq. (4), while $\underline{\underline{\mathbf{M}}}$ is the tensor given by $\underline{\underline{\mathbf{M}}} = \underline{\underline{T}}_{\mathrm{M}} \times \mathbf{r}$ appearing in Eq. (5). The Einstein summation convention has been used. The first term appearing in both Eqs. (24a) and (24b) is the time rate of change of the pertaining momentum density, while the second term gives the gradient of the density flux. Integrating Eqs. (24a) and (24b) over regions of space gives, for the first terms, the time rate of change of the total linear or angular momentum within a prescribed volume. The spatial derivatives in the second terms can be replaced by surface integrals by invoking the divergence theorem, giving the terms appearing on the right-hand side of Eqs. (4) and (5). They can now be interpreted as density fluxes across the prescribed surface.

In light of this, the meaning of Eqs. (4) and (5) becomes clearer. The surface integrals on the right-hand side give the flux of the appropriate momentum density across a surface bounding the scattering object. By virtue of the continuity equations, which, in turn, are expressions of underlying conservation laws, this flux is equivalent to the rate of change of the total linear or angular momentum inside the surface that occurs as a result of the scattering process. Since total angular (or linear) momentum is conserved, the rates of change of electromagnetic angular (or linear) momentum are equated to the mechanical torques (or forces) experienced by the particle.

These considerations suggest that the interactions between beams and particles may be more complicated than initially thought. Light beams *do not* possess a fixed quantity of momentum that can be partially transferred to scattering bodies in such a way as to increase the momentum of the particle at the cost of the beam. On the contrary, the total momentum of an unperturbed beam is proportional to its length. In the frequency domain, therefore, it is infinite, and making statements about its conservation is not meaningful. What determines the torque experienced by the particle is the net angular momentum *flux* arising as a consequence of scattering, and this need not be in accordance with intuition.

This last point can be appreciated by considering a more generally accepted example. When an elongated particle (prolate spheroid, cylinder, etc.) is held horizontally in a linearly polarized Gaussian beam, it will orient itself with its long axis parallel to the electric field polarization. If it is rotated about the beam axis away from the equilibrium orientation and held in that position, it will feel a restoring torque that is the result of an angular momentum flux across a surface bounding the particle. It is therefore known that a beam that does not carry angular momentum can, in the presence of a scattering particle, give rise to a linearly increasing angular momentum density within a surface bounding the particle. It would seem, therefore, not so very unusual that a beam carrying angular momentum in one sense should be capable of imparting a relatively small torque on a particle of the opposite sense.

The situation is further complicated by the controversy that has, for some time, surrounded the existence, or otherwise, of angular momentum in circularly polarized light (see Ref. 32 for a review of the debate). It is commonly accepted that although circularly polarized *plane* waves do not carry angular momentum, finite sections of them do, and that the transport of angular momentum in circularly polarized light occurs as a consequence of boundary effects. The fact that the counterrotation of oblate spheroids observed above, occurs in a size range in which the size of the beam waist falls between two radii of the spheroid is,

therefore, also likely to be significant. In this respect, we would expect the behavior in circularly polarized beams to differ from that in beams with phase singularities, i.e., optical vortices, in which transfer of angular momentum will occur irrespective of the existence of boundaries.

The above paragraphs are intended to suggest that, although the counterrotation of certain sizes of oblate spheroids in circularly polarized beams predicted here may appear to be against intuition, it is not significantly more unusual than other, more generally accepted, phenomena. However, the precise nature of the mechanisms giving rise to these results remains unclear and requires further analysis.

Another, potentially fruitful, avenue of future investigation involves the coupling of rotational and translational motion suggested by Fig. 12. In this case, the rotation of an oblate spheroid about the beam axis results in significant changes in the vertical component of force on the particle. In fact, although not demonstrated here, this will be equally true for the rotation of any principal axis of any spheroid from its equilibrium orientation. Similarly, translating the center of a particle away from its equilibrium position will induce a torque as well as a restoring force. This has implications for the dynamics of trapped anisotropic particles and will have consequences both for the spectrum of Brownian motion that will be observed and for the behavior of such particles in moving traps. An understanding of this coupling will be of great importance when using dynamic holographic techniques to assemble anisotropic nanoparticles into complex structures.

5. CONCLUSIONS

We have presented a study of the forces and torques on spheroidal particles in Gaussian optical traps calculated using T matrix theory. In linearly polarized beams, the general principle that operates is that of maximizing the overlap between the particle and the most intense parts of the beam. Thus, prolate spheroids generally align with the symmetry axis parallel to the beam; whereas oblate spheroids always assume a perpendicular orientation. A second principle operating is that of aligning the long axis of the particle with the polarization direction. For oblate particles, both conditions may be satisfied simultaneously. However, for the prolate case, alignment with the polarization vector is only possible for small particles, i.e., those whose long axis is small compared with the beam waist. In circularly polarized light, oblate particles experience a torque about the beam axis leading to continuing rotation. However, the sense of the rotation varies depending on the relative dimensions of the particle and the beam waist.

APPENDIX A: GAUSSIAN BEAM REPRESENTATION

The coefficients in the VSWF expansion of the fifth-order Davis beam approximation to the incident Gaussian beam are given by

$$a_{1n} = a_{-1n} = b_{1n} = -b_{1n} = -(-i)^{n+1}[4\pi(2n+1)]^{1/2} g_{5,n}, \tag{A1}$$

where

$$g_{5,n} = g_{3,n} + \exp[-s^2(n-1)(n+2)](n-1)^2(n+2)^2 s^8 \times [10 - 5(n-1)(n+2)s^2 + 0.5(n-1)^2(n+2)^2 s^4], \tag{A2}$$

$$g_{3,n} = g_{1,n} + \exp[-s^2(n-1)(n+2)](n-1)(n+2)s^4 \times [3 - (n-1)(n+2)s^2], \tag{A3}$$

$$g_{1,n} = \exp[-s^2(n-1)(n+2)]. \tag{A4}$$

ACKNOWLEDGMENTS

The authors thank J. P. Barton and Massimo Antognozzi for helpful comments. They are grateful to the United Kingdom Research Councils (RCUK) for financial support. This work was performed as part of the Basic Technology project: A Dynamic Holographic Assembler.

S. Hanna's e-mail address is s.hanna@bristol.ac.uk.

REFERENCES

1. A. Ashkin, J. M. Dziedzic, J. E. Bjorkholm, and S. Chu, "Observation of a single-beam gradient force optical trap for dielectric particles," Opt. Lett. **11**, 288–290 (1986).
2. J. E. Molloy and M. J. Padgett, "Lights, action: optical tweezers," Contemp. Phys. **43**, 241–258 (2002).
3. D. G. Grier, "A revolution in optical manipulation," Nature **424**, 810–816 (2003).
4. S. H. Simpson and S. Hanna, "Numerical calculation of interparticle forces arising in association with holographic assembly," J. Opt. Soc. Am. A **23**, 1419–1431 (2006).
5. S. Bayoudh, T. A. Nieminen, N. R. Heckenberg, and H. Rubinsztein-Dunlop, "Orientation of biological cells using plane-polarized Gaussian beam optical tweezers," J. Mod. Opt. **50**, 1581–1590 (2003).
6. A. Ashkin, "Acceleration and trapping of particles by radiation pressure," Phys. Rev. Lett. **24**, 156–159 (1970).
7. K. Ren, G. Grehan, and G. Gouesbet, "Radiation pressure forces exerted on a particle arbitrarily located in a Gaussian beam by using the generalized Lorenz–Mie theory, and associated resonance effects," Opt. Commun. **108**, 343–354 (1994).
8. J. P. Barton, D. R. Alexander, and S. A. Schaub, "Theoretical determination of net radiation force and torque for a spherical particle illuminated by a focused laser beam," J. Appl. Phys. **66**, 4594–4602 (1989).
9. C. J. F. Böttcher, *Theory of Electric Polarization*, Vol. 1 of Dielectrics in Static Fields, 2nd ed. (Elsevier, 1973).
10. J. D. Jackson, *Classical Electrodynamics*, 2nd ed. (Wiley, 1975).
11. A. I. Bishop, T. A. Nieminen, N. R. Heckenberg, and H. Rubinsztein-Dunlop, "Optical application and measurement of torque on microparticles of isotropic nonabsorbing material," Phys. Rev. A **68**, 033802 (2003).
12. K. D. Bonin, B. Kourmanov, and T. G. Walker, "Light torque nanocontrol, nanomotors and nanorockers," Opt. Express **10**, 984–989 (2002).
13. P. Galajda and P. Ormos, "Orientation of flat particles in optical tweezers by linearly polarized light," Opt. Express **11**, 446–451 (2003).
14. A. La Porta and M. D. Wang, "Optical torque wrench: angular trapping, rotation, and torque detection of quartz microparticles," Phys. Rev. Lett. **92**, 190801 (2004).

15. J.-S. Kim and S.-W. Kim, "Dynamic motion analysis of optically trapped nonspherical particles with off-axis position and arbitrary orientation," Appl. Opt. **39**, 4327–4332 (2000).
16. R. C. Gauthier, "Theoretical investigation of the optical trapping force and torque on cylindrical micro-objects," J. Opt. Soc. Am. B **14**, 3323–3333 (1997).
17. R. C. Gauthier, "Optical levitation and trapping of a micro-optic inclined end-surface cylindrical spinner," Appl. Opt. **40**, 1961–1973 (2001).
18. M. I. Mishchenko, L. D. Travis, and A. A. Lacis, *Scattering, Absorption and Emission of Light by Small Particles* (Cambridge U. Press, 2002).
19. L. Tsang, J. A. Kong, and R. T. Shin, *Theory of Microwave Remote Sensing* (Wiley, 1985).
20. O. Moine and B. Stout, "Optical force calculations in arbitrary beams by use of the vector addition theorem," J. Opt. Soc. Am. B **22**, 1620–1631 (2005).
21. G. Gouesbet, J. A. Lock, and G. Grehan, "Partial wave representations of laser beams for use in light scattering calculations," Appl. Opt. **34**, 2133–2143 (1995).
22. G. Gouesbet, "Partial-wave expansions and properties of axisymmetric light beams," Appl. Opt. **35**, 1543–1555 (1996).
23. E. Anderson, Z. Bai, C. Bischof, S. Blackford, J. Demmel, J. Dongarra, J. Du Croz, A. Greenbaum, S. Hammarling, A. McKenney, and D. Sorensen, *LAPACK Users' Guide*, 3rd ed. (Society for Industrial and Applied Mathematics, 1999).
24. F. Melia, *Electrodynamics* (The University of Chicago Press, 2001).
25. P. L. Marston and J. H. Crichton, "Radiation torque on a sphere caused by a circularly-polarized electromagnetic wave," Phys. Rev. A **30**, 2508–2516 (1984).
26. S. Chang and S. S. Lee, "Optical torque exerted on a homogeneous sphere levitated in the circularly polarized fundamental-mode of a laser beam," J. Opt. Soc. Am. B **2**, 1853–1860 (1985).
27. G. Gouesbet, B. Maheu, and G. Grehan, "Light scattering from a sphere arbitrarily located in a Gaussian beam, using a Bromwich formulation," J. Opt. Soc. Am. A **5**, 1427–1443 (1988).
28. P. Barber, "Resonance electromagnetic absorption by nonspherical dielectric objects," IEEE Trans. Microwave Theory Tech. **25**, 373–381 (1977).
29. A. Mugnai and W. Wiscombe, "Scattering of radiation by moderately nonspherical particles," J. Atmos. Sci. **37**, 1291–1307 (1980).
30. V. Varadan, A. Lakhtakia, and V. Varadan, "Scattering by 3-dimensional anisotropic scatterers," IEEE Trans. Antennas Propag. **37**, 800–802 (1989).
31. T. G. M. van der Ven, *Colloidal Hydrodynamics* (Academic, 1989).
32. A. M. Stewart, "Angular momentum of the electromagnetic field: the plane wave paradox resolved," Eur. J. Phys. **26**, 635–641 (2005).
33. R. A. Beth, "Mechanical detection and measurement of the angular momentum of light," Phys. Rev. **50**, 115–125 (1936).
34. M. E. J. Friese, J. Enger, H. Rubinsztein-Dunlop, and N. R. Heckenberg, "Optical angular-momentum transfer to trapped absorbing particles," Phys. Rev. A **54**, 1593–1596 (1996).
35. M. E. J. Friese, T. A. Nieminen, N. R. Heckenberg, and H. Rubinsztein-Dunlop, "Optical alignment and spinning of laser-trapped microscopic particles," Nature **394**, 348–350 (1998).
36. D. Benito, S. H. Simpson, and S. Hanna are preparing a paper to be called "FDTD calculations of forces and torques on ellipsoidal particles."
37. S. M. Barnett, "Optical angular-momentum flux," J. Opt. B: Quantum Semiclassical Opt. **4**, S7–S16 (2002).